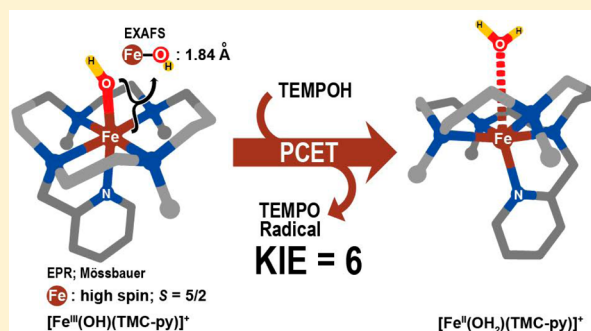


Characterization of the Fleeting Hydroxoiron(III) Complex of the Pentadentate TMC-py Ligand

Wei-Min Ching,^{†,‡} Ang Zhou,[†] Johannes E. M. N. Klein,[†] Ruixi Fan,[‡] Gerald Knizia,[§] Christopher J. Cramer,^{*,‡} Yisong Guo,^{*,‡} and Lawrence Que, Jr.^{*,†}[†]Department of Chemistry and Center for Metals in Biocatalysis and [‡]Department of Chemistry, Supercomputing Institute, and Chemical Theory Center, University of Minnesota, Minneapolis, Minnesota 55455, United States[‡]Department of Chemistry, Carnegie Mellon University, Pittsburgh, Pennsylvania 15213, United States[§]Department of Chemistry, Pennsylvania State University, 401A Chemistry Bldg; University Park, Pennsylvania 16802, United States

S Supporting Information

ABSTRACT: Nonheme mononuclear hydroxoiron(III) species are important intermediates in biological oxidations, but well-characterized examples of synthetic complexes are scarce due to their instability or tendency to form μ -oxodiiron(III) complexes, which are the thermodynamic sink for such chemistry. Herein, we report the successful stabilization and characterization of a mononuclear hydroxoiron(III) complex, $[\text{Fe}^{\text{III}}(\text{OH})(\text{TMC-py})]^{2+}$ (**3**; TMC-py = 1-(pyridyl-2'-methyl)-4,8,11-trimethyl-1,4,8,11-tetrazacyclotetradecane), which is directly generated from the reaction of $[\text{Fe}^{\text{IV}}(\text{O})(\text{TMC-py})]^{2+}$ (**2**) with 1,4-cyclohexadiene at -40°C by H-atom abstraction. Complex **3** exhibits a UV spectrum with a λ_{max} at 335 nm ($\epsilon \approx 3500 \text{ M}^{-1} \text{ cm}^{-1}$) and a molecular ion in its electrospray ionization mass spectrum at m/z 555 with an isotope distribution pattern consistent with its formulation. Electron paramagnetic resonance and Mössbauer spectroscopy show **3** to be a high-spin Fe(III) center that is formed in 85% yield. Extended X-ray absorption fine structure analysis reveals an Fe–OH bond distance of 1.84 Å, which is also found in $[(\text{TMC-py})\text{Fe}^{\text{III}}-\text{O}-\text{Cr}^{\text{III}}(\text{OTf})_3]^+$ (**4**) obtained from the reaction of **2** with $\text{Cr}(\text{OTf})_2$. The $S = 5/2$ spin ground state and the 1.84 Å Fe–OH bond distance are supported computationally. Complex **3** reacts with 1-hydroxy-2,2,6,6-tetramethylpiperidine (TEMPOH) at -40°C with a second-order rate constant of $7.1 \text{ M}^{-1} \text{ s}^{-1}$ and an OH/OD kinetic isotope effect value of 6. On the basis of density functional theory calculations, the reaction between **3** and TEMPOH is classified as a proton-coupled electron transfer as opposed to a hydrogen-atom transfer.



■ INTRODUCTION

Since 2003 high-valent iron(IV)-oxo intermediates have been trapped and characterized for a number of nonheme iron enzymes.^{1–4} Such high-valent intermediates serve various roles, most importantly the cleavage of C–H bonds for the functionalization of substrates. The first well-documented example of an enzymatic oxoiron(IV) species is intermediate J of taurine dioxygenase, which is shown to perform the oxidation of the substrate C–H bond. Transformations at high-valent oxoiron active sites are expected to proceed via hydrogen atom transfer (HAT) reactions, where the oxoiron(IV) moiety is initially reduced to a hydroxoiron(III) species.

The field of bioinorganic chemistry has provided great insight into the area of nonheme oxoiron(IV) chemistry, particularly with respect to the characterization of their structural, spectroscopic, and reactivity properties.^{5–9} Such studies to date have almost exclusively focused on the high-valent oxoiron(IV) intermediates with less emphasis on the properties of the corresponding hydroxoiron(III) complexes, which are frequently proposed to form immediately after the initial

HAT.^{4,10} The small number of reports in this field may be attributed to the challenges posed by such complexes due to their (thermal) instability.

Masuda and Borovik have reported the only crystal structures of nonheme hydroxoiron(III) complexes.^{11–13} These complexes have been stabilized by the introduction of H-bonding moieties in the second coordination sphere in the design of the supporting ligand (Figure 1). In addition, our group has trapped the $[\text{Fe}^{\text{III}}(\text{OH})(\text{TMG}_3\text{tren})]^{2+}$ species ($\text{TMG}_3\text{tren} = 1,1,1\text{-tris}\{2\text{-[N2-(1,1,3,3-tetramethylguanidino)]ethyl}\}$ amine) obtained from the reaction of $[\text{Fe}^{\text{IV}}(\text{O})(\text{TMG}_3\text{tren})]^{2+}$ with 1,4-cyclohexadiene (CHD) and characterized the hydroxoiron(III) complex using electron paramagnetic resonance (EPR), Mössbauer, and X-ray absorption spectroscopy.¹⁴ The tripodal TMG_3tren ligand does not provide H-bonding moieties in the second coordination sphere like the other two complexes mentioned above but instead has sterically bulky tetramethyl-

Received: June 8, 2017

Published: August 31, 2017



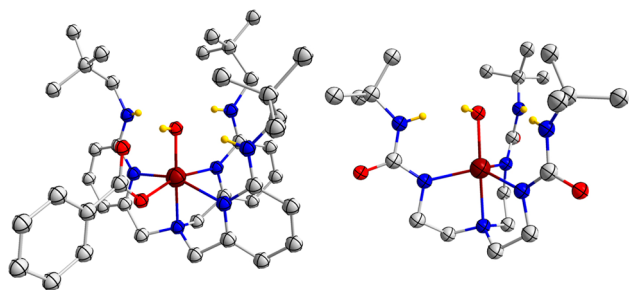
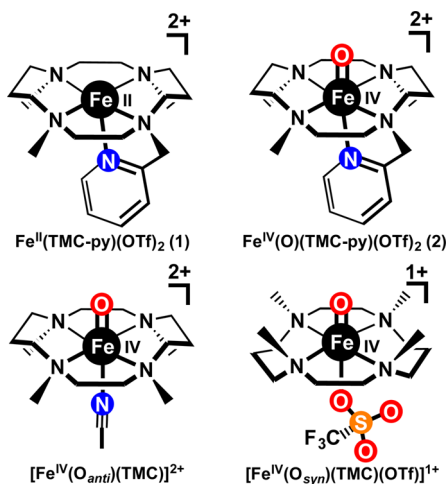


Figure 1. Crystal structures of hydroxoiron(III) complexes reported by Masuda¹¹ (left) and Borovik¹³ (right).

guanidino substituents that shield the hydroxo ligand and prolong the lifetime of the complex.

The relatively high stability of nonheme oxoiron(IV) complexes supported by the macrocyclic tetramethylcyclam ligand (TMC) or a pentadentate variant bearing an appended pyridine group (TMC-py; see Chart 1)^{5,15,16} has led us to

Chart 1



investigate whether the corresponding hydroxoiron(III) complexes might have sufficient lifetimes to be trapped and characterized. Indeed, on the one hand, Nam and co-workers have provided some evidence for the formation of the one-electron reduced oxoiron(III) complex, but it is not very stable.^{17,18} On the other hand, Borovik and Fout have been successful in crystallizing such oxoiron(III) complexes with suitable ligand design.^{12,19} In the present report, we demonstrate that the $\text{Fe}^{\text{III}}(\text{OH})(\text{TMC-py})(\text{OTf})_2$ (3) complex can be generated from the reaction of $[\text{Fe}^{\text{IV}}(\text{O})(\text{TMC-py})]^{2+}$ (2) with CHD at -40°C and characterized by a variety of spectroscopic methods. In addition, we also show that 3 can oxidize 1-hydroxy-2,2,6,6-tetramethylpiperidine (TEMPO-H/D) and exhibits a moderately high kinetic isotope effect (KIE) for this reaction.

EXPERIMENTAL SECTION

General Information. All reagents and solvents were purchased from commercial sources and used as received unless specified. *n*-PrCN was further purified using Na_2CO_3 and KMnO_4 . The mixture was heated at 75°C for several hours and distilled under Ar atmosphere.²⁰ The preparations for $\text{Fe}(\text{OTf})_2(\text{MeCN})_2$ (^{56}Fe or ^{57}Fe),²¹ $\text{Cr}(\text{OTf})_2(\text{MeCN})_2$,²² TEMPOH,²³ TEMPOD,²⁴ and TMC-py,¹⁶ as well as iodosylbenzene ($\text{C}_6\text{H}_5\text{IO}$) and its ^{18}O isotopomer,²⁵

were performed following published procedures. Stock solutions of $\text{Fe}^{\text{IV}}(\text{O})(\text{TMC-py})(\text{OTf})_2$ (2) and $\text{Fe}^{\text{IV}}(^{18}\text{O})(\text{TMC-py})(\text{OTf})_2$ were kept in the -40°C refrigerator in a N_2 -filled glovebox. Samples for EPR experiments on $\text{Fe}^{\text{III}}(\text{OH})(\text{TMC-py})(\text{OTf})_2$ (3) were prepared in MeCN under N_2 atmosphere at -40°C and then transferred via gastight syringe to precooled EPR tubes and frozen immediately in liquid N_2 . Corresponding extended X-ray absorption fine structure (EXAFS) and Mössbauer samples were quickly loaded into sample cups and then frozen in liquid N_2 . All moisture- and oxygen-sensitive compounds and solvent were prepared using standard Schlenk-line techniques and N_2 -filled glovebox.

UV-vis absorption spectra were recorded on an HP 8453A diode array spectrometer. Low-temperature visible spectra were obtained using a cryostat from UNISOKU Scientific Instruments, Japan. Electrospray ionization mass spectrometry (ESI-MS) was performed on a Finnigan LCQ ion trap mass spectrometer. ^1H NMR spectra were collected on a Bruker 400 MHz spectrometer. X-band EPR spectra were measured on a Bruker Elexsys E-500 spectrometer equipped with an Oxford ESP-910 cryostat. Mössbauer spectra were recorded with home-built spectrometers using Janis Research Super-VariTemp dewars. Mössbauer spectral simulations were performed using the WMOSS software package (SEE Co., Edina, MN) and SpinCount software.²⁶ Isomer shifts are quoted relative to Fe metal at 298 K. All Mössbauer figures were prepared using SpinCount software. EPR simulations were performed by using the SpinCount software.²⁶ The spin Hamiltonian used for the EPR and Mössbauer simulations in Figures 4, 5, and S10 is

$$\hat{H} = D \left[\left(\hat{S}_z^2 - \frac{35}{4} \right) + \frac{E}{D} (\hat{S}_x^2 - \hat{S}_y^2) \right] + \beta \hat{\mathbf{S}} \cdot \mathbf{g} \cdot \mathbf{B} + \hat{\mathbf{S}} \cdot \mathbf{A} \cdot \hat{\mathbf{I}} - g_{\text{H}} \beta_{\text{H}} \hat{\mathbf{B}} \cdot \hat{\mathbf{I}} + \hat{H}_{\text{Q}} \quad (1)$$

where $\hat{H}_{\text{Q}} = \frac{eQV_{zz}}{12} \left[\hat{I}_z^2 - \frac{15}{4} + \eta (\hat{I}_x^2 - \hat{I}_y^2) \right]$.

X-ray Absorption Spectroscopy (XAS). XAS data were collected at Beamline 7-3 at the Stanford Synchrotron Radiation Lightsources (SSRL) of SLAC National Accelerator Laboratory. Fe K-edge XAS data were collected over the energy range of 6.9–8.0 keV on frozen samples maintained at 10 K. An Fe foil spectrum was measured simultaneously for internal energy calibration using the first inflection point of the K-edge energy (7112.0 eV). Data were obtained in the fluorescence mode using a solid-state germanium detector (Canberra).

Data reduction, averaging, and normalization were performed using the program EXAFSPAK.²⁷ The coordination number of a given shell was a fixed parameter and was varied iteratively in integer steps, while the bond lengths (*R*) and mean-square deviation (σ^2) were allowed to freely float. The amplitude reduction factor was fixed at 0.9, while the edge-shift parameter E_0 was allowed to float as a single value for all shells. The pre-edge features were fitted using the Fityk program²⁸ with pseudo-Voigt functions composed of 50:50 Gaussian/Lorentzian functions.

Preparation of $\text{Fe}^{\text{II}}(\text{TMC-py})(\text{OTf})_2$ (1). $\text{Fe}^{\text{II}}(\text{TMC-py})(\text{OTf})_2$ (1) was synthesized by a published procedure.¹⁶ The ^1H NMR spectrum of 1 at -40°C showed well-resolved signals. The three methyl groups of 1 were assigned by peak integration²⁹ (see Figure S1). ^1H NMR (400 MHz, CD_3CN , 233 K): δ 443.9 (1H), 440.2 (1H), 327.9 (1H), 264.3 (1H), 258.8 (1H), 239.3 (1H), 226.7 (3H, NMe), 207.5 (3H, NMe), 160.3 (1H), 143.3 (1H), 143.3 (1H), 126.5 (1H), 117.7 (3H, NMe), 95.1 (1H), 80.7 (2H), 47.1 (1H), 38.2 (1H), 32.2 (1H), 23.3 (1H), 14.1 (1H), 5.1 (1H), 2.4 (2H), -10.6 (1H), -19.2 (1H), -26.2 (1H), -37.5 (1H), -116.9 (1H). ESI-MS: Calcd for $\text{C}_{20}\text{H}_{35}\text{F}_3\text{N}_5\text{O}_3\text{S}_1\text{Fe}_1$ $\{\text{M-OTf}\}^+$, 537.9; Found: 538.2. ^{57}Fe -labeled 1 was synthesized by the same procedure¹⁶ but was performed on a smaller scale using 22 mg of $^{57}\text{Fe}(\text{OTf})_2(\text{MeCN})_2$ as the starting material.

Generation of $\text{Fe}^{\text{IV}}(\text{O})(\text{TMC-py})(\text{OTf})_2$ (2). $\text{Fe}^{\text{IV}}(\text{O})(\text{TMC-py})(\text{OTf})_2$ (2) was generated by the reaction of 1 with 2 equiv of PhIO according to the published procedure.¹⁶ Solid 2 was obtained by adding 30 mL of anhydrous diethyl ether into a 48 mM solution of 2 in 3 mL of MeCN at -40°C . The precipitate was washed with

anhydrous diethyl ether several times, dried under vacuum for 2 min, and then stored at $-40\text{ }^{\circ}\text{C}$. ^{18}O -labeled **2** for the ESI-MS experiments was generated using $\text{C}_6\text{H}_5\text{I}^{18}\text{O}$ as the oxidant. ^1H NMR (400 MHz, CD_3CN , 298 K; Figure S2): δ 76.0 (1H), 59.1 (1H), 52.2 (1H), 43.1 (2H), 39.7 (1H), 29.8 (1H), 27.3 (1H), 20.1 (1H), 10.9 (1H), 6.3 (1H), -4.6 (1H), -19 (1H), -37.4 , -38.2 (7H, NMe, NMe), -43.7 (3H, NMe), -71.4 (1H), -80 (1H), -149.5 (1H), -161.4 (1H), 166.8 (1H), 170.7 (1H). Six other proton signals were not found and may be significantly broadened by the paramagnetic center. ESI-MS: Calcd for $\text{C}_{20}\text{H}_{35}\text{F}_3\text{N}_5\text{O}_4\text{S}_1\text{Fe}_1$ $\{\text{M-OTf}\}^+$, 554.2; Found: 554.0. Calcd for $\text{C}_{20}\text{H}_{35}\text{F}_3\text{N}_5^{18}\text{O}_4\text{S}_1\text{Fe}_1$ $\{\text{M-OTf}\}^+$, 556.2; Found: 556.1.

Generation of $\text{Fe}^{\text{III}}(\text{OH})(\text{TMC-py})(\text{OTf})_2$ (3**).** $\text{Fe}^{\text{III}}(\text{OH})(\text{TMC-py})(\text{OTf})_2$ (**3**) was generated at $-40\text{ }^{\circ}\text{C}$ from the reaction of **2** (0.5 mM solution in MeCN) with 200 equiv of CHD under anaerobic conditions for 40 min. The reactions were monitored by the disappearance of the characteristic near-IR band of **2** at 834 nm and the appearance of a new absorbance band at 335 nm ($\epsilon \approx 3500\text{ M}^{-1}\text{ cm}^{-1}$), which was assigned to $\text{Fe}^{\text{III}}(\text{OH})(\text{TMC-py})(\text{OTf})_2$ (**3**). The yield of **3** was estimated to be 80%, based on the amount of decamethylferrocenium ion produced in the reaction of **3** with 1 equiv of decamethylferrocene (relative to the amount of **2** used in its reaction with CHD), which was calibrated by the reaction of $(\text{NH}_4)_2\text{Ce}^{\text{IV}}(\text{NO}_3)_6$ with decamethylferrocene under the same conditions (see Figure S3).

Generation of $(\text{TMC-py})\text{Fe}^{\text{III}}\text{O-Cr}^{\text{III}}(\text{OTf})_4(\text{MeCN})$ (4**).** $(\text{TMC-py})\text{Fe}^{\text{III}}\text{O-Cr}^{\text{III}}(\text{OTf})_4(\text{MeCN})$ (**4**) was generated at $-40\text{ }^{\circ}\text{C}$ by the reaction of **2** (0.45 mM solution in MeCN) with 1.25 equiv of $\text{Cr}^{\text{III}}(\text{OTf})_2$ under anaerobic conditions. The characteristic near-IR band of **2** at 834 nm decreased immediately, and this decrease was accompanied by the appearance of new bands at 382, 450, and 557 nm ($\epsilon \approx 3800$, 3200, and $920\text{ M}^{-1}\text{ cm}^{-1}$, respectively), very similar to the spectral pattern recently reported for $(\text{MeCN})(\text{TMC})\text{Fe}^{\text{III}}\text{O-anti-Cr}^{\text{III}}(\text{OTf})_4(\text{MeCN})$.^{22,30} ^{18}O -labeled **4** was generated similarly by using ^{18}O -labeled **2** as starting material (64% ^{18}O -labeled). ESI-MS: the molecular ion peak was observed at m/z 903.8, which shifted to m/z 905.8 upon ^{18}O -labeling of the oxo atom in the precursor. Calcd for $\text{C}_{22}\text{H}_{35}\text{F}_3\text{N}_5\text{O}_{10}\text{S}_3\text{Fe}_1\text{Cr}_1$ $\{\text{M-OTf-MeCN}\}^+$, 904.0 (see Figures S4–S8).

Reaction of $\text{Fe}^{\text{III}}(\text{OH})(\text{TMC-py})(\text{OTf})_2$ (3**) with TEMPOH/D.** $\text{Fe}^{\text{III}}(\text{OH})(\text{TMC-py})(\text{OTf})_2$ (**3**) was generated in situ for each experiment at $-40\text{ }^{\circ}\text{C}$ as described above. Stock solutions of TEMPOH and TEMPOD were prepared in 1 mL of MeCN (2.1×10^{-1} and $2.54 \times 10^{-1}\text{ M}$, respectively) within a glovebox and kept in a $0\text{ }^{\circ}\text{C}$ ice bath outside of the glovebox. To the $\text{Fe}^{\text{III}}(\text{OH})(\text{TMC-py})(\text{OTf})_2$ (**3**) solution in MeCN was introduced 10–50 equiv of TEMPOH or 10–100 equiv of TEMPOD at $-40\text{ }^{\circ}\text{C}$. The reaction products were analyzed by ESI-MS and EPR spectroscopy, revealing a peak at m/z 538 corresponding to $[\text{Fe}^{\text{II}}(\text{TMC-py})(\text{OTf})]^+$ and an EPR signal corresponding to the TEMPO radical (93% yield; see Figure S9).

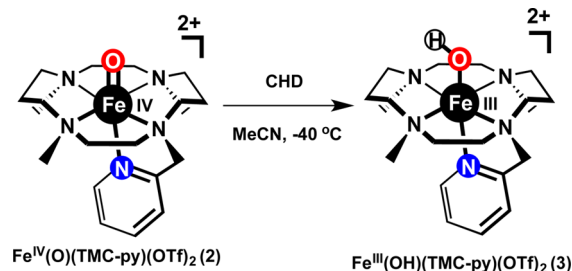
Computational Details. Geometry optimizations and single-point calculations were performed using the electronic structure code Turbomole v7.0.1.^{31–33} Geometry optimizations were performed using the M06-L functional³⁴ in combination with the def2-TZVP basis set for Fe and the def2-SVP basis set for all other elements.³⁵ Single-point energies were computed at these optimized structures using the def2-TZVPP basis set³⁵ in combination with the M06-L and the M06³⁶ functionals. In all calculations, acetonitrile solvation ($\epsilon = 35.88$ ³⁷ and $n = 1.344$ ^{38,39}) was accounted for using the COSMO solvation model.⁴⁰ Electronic energies reported include an outlying charge correction.⁴¹ Frequency calculations were performed to confirm the nature of stationary points resulting in no imaginary frequencies for minima and a single imaginary frequency for transition-state (TS) structures. To obtain thermal contributions to thermochemical quantities, frequencies were computed using frozen charges (NumForce –cosmo option), derivatives of quadrature weight, and small frequencies were raised to 100 cm^{-1} .^{42,43} Frequencies were used without scaling. Free energies are referenced to a 1 M standard state in solution (233.15 K) and include a concentration-change term relative to a 1 bar gaseous standard state of $RT \ln(19.1) = 1.37\text{ kcal mol}^{-1}$.⁴⁴

All calculations use grid $m5$ and were accelerated by the MARI-J⁴⁵ approach using Weigend's fitting basis sets.⁴⁶ Because of the poor self-consistent field (SCF) convergence of some calculations, an initial level shift of 0.5 was introduced ($\text{\$scf}(\text{orbitalshift automatic} = 0.5)$) in all calculations. The VdW complexes before and after the transition state were obtained using the DRC tool in Turbomole (DRC –t 150 –f).⁴⁷ Structural depictions and intrinsic bond orbital (IBO, *iboexp* was set to 2)⁴⁸ analyses were made using IboView.^{49,50}

RESULTS AND DISCUSSION

1. Generation of $[\text{Fe}^{\text{III}}(\text{OH})(\text{TMC-py})](\text{OTf})_2$ (3**).** The reaction of $\text{Fe}^{\text{IV}}(\text{O})(\text{TMC-py})(\text{OTf})_2$ (**2**) with 200 equiv of CHD (Scheme 1) in MeCN at $-40\text{ }^{\circ}\text{C}$ was monitored by UV–

Scheme 1. Reaction of $\text{Fe}^{\text{IV}}(\text{O})(\text{TMC-py})(\text{OTf})_2$ (**2**) with 1,4-Cyclohexadiene



vis spectroscopy, and complete consumption of **2** was observed within 40 min. The light green solution of **2** turned light yellow, corresponding to the loss of its characteristic near-IR feature at 834 nm concomitant with an increase in absorbance at 335 nm ($\epsilon \approx 3500\text{ M}^{-1}\text{ cm}^{-1}$; Figure 2). As shown in the inset for

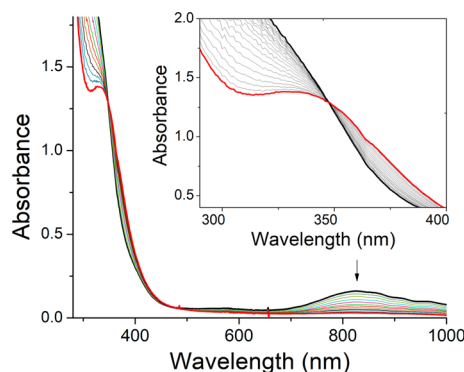


Figure 2. UV–vis spectral changes upon addition of 200 equiv of CHD into a 0.5 mM solution of $\text{Fe}^{\text{IV}}(\text{O})(\text{TMC-py})(\text{OTf})_2$ (**2**, black line) to form $[\text{Fe}^{\text{III}}(\text{OH})(\text{TMC-py})]^{2+}$ (**3**, red line) in MeCN at $-40\text{ }^{\circ}\text{C}$. (inset) Expanded 280–400 nm region to show the isosbestic point associated with the reaction.

Figure 2, there is an isosbestic point in the conversion of **2** to its product **3**. We propose that **3** corresponds to $[\text{Fe}^{\text{III}}(\text{OH})(\text{TMC-py})]^{2+}$, which would be formed by HAT from CHD by **2**. The formulation for **3** was corroborated by the appearance of a dominant peak at m/z 555 in its ESI-MS (Figure 3) with a mass and isotope distribution pattern consistent with the $[\text{Fe}^{\text{III}}(\text{OH})(\text{TMC-py})(\text{OTf})]^+$ ion. Moreover, the m/z 555 peak shifted to m/z 557 with the use of ^{18}O -labeled **2** (64% ^{18}O content). Furthermore, **3** was generated with a yield estimated to be $\sim 80\%$ based on the amount of decamethylferrocenium ion formed upon addition of decamethylferrocene to the reaction solution (see Figure S3).

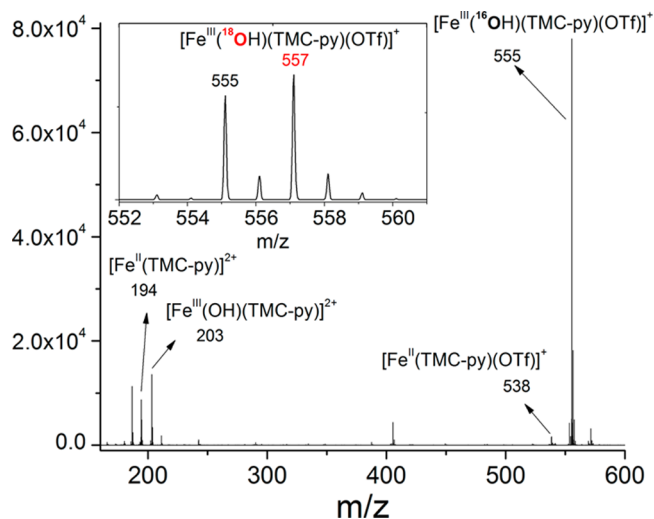


Figure 3. ESI-MS spectrum of the solution after the reaction of $\text{Fe}^{\text{IV}}(^{16}\text{O})(\text{TMC-py})(\text{OTf})_2$ (**2**) with CHD in MeCN at -40°C . (inset) Isotopic pattern of the $[\text{Fe}^{\text{III}}(^{18}\text{OH})(\text{TMC-py})(\text{OTf})]^+$ ion with 64% isotope enrichment. ESI-MS spectra were obtained with the carrier gas set at 40°C .

Complex **3** was further characterized by EPR and Mössbauer spectroscopy. The EPR spectrum measured on a sample containing **3** exhibits signals with observed g values at 4.3 and 9.0 (Figure 4), indicative of a rhombic ($E/D \approx 0.3$) high-spin ($S = 5/2$) iron(III) species. The $g = 4.3$ resonance originates from the middle Kramers doublet of this $S = 5/2$ species, while the $g = 9.03$ resonance consists of signals from both the ground and upper Kramers doublets of the same $S = 5/2$ species. The broadness of the observed EPR signals from **3** likely originates, in part, from an E/D distribution (see the Supporting Information for more discussion), probably resulting from slight inhomogeneity of the structure of **3**. The magnitude of the axial zero-field splitting parameter, D , was found to be 1.1 cm^{-1} from the temperature dependence of the intensity of the $g = 4.3$ resonance, but the sign of D could not be readily determined due to the high rhombicity of the spin system ($E/D \approx 0.3$).

Mössbauer spectra on a sample containing **3** measured at different magnetic fields applied parallel to the γ -rays and at different temperatures further confirm the assignment of **3** as a typical high-spin ferric species with $E/D \approx 0.3$, isomer shift $\delta = 0.44\text{ mm/s}$, and an isotropic A tensor ($A_x/g_n\beta_n = A_y/g_n\beta_n = A_z/g_n\beta_n = -20.7\text{ T}$). More specifically, the low-field (45 mT) spectrum measured at 1.8 K shows a six-line pattern (Figure 5a), which originates from the ground Kramers doublet of an $S = 5/2$ species having a uniaxial magnetic behavior (the spectrum is only sensitive to the y ($D > 0$) or z ($D < 0$) component of the internal field). Increasing the temperature to 4.2 K results in the appearance of spectral features (indicated by solid arrows in Figure 5b) belonging to the middle Kramers doublet of the same $S = 5/2$ species. Furthermore, the 10 K spectrum (Figure 5c) clearly shows the spectral features belonging to the upper Kramers doublet (indicated by dashed arrows), which also shows a uniaxial magnetic behavior. The relative intensities of the spectral features belonging to the different Kramers doublets provide an accurate measure of the magnitude of the axial zero-field splitting parameter D , which in this case equals 1.1 cm^{-1} . However, the sign of D cannot be reliably determined for an $S = 5/2$ system with $E/D \approx 0.3$. The

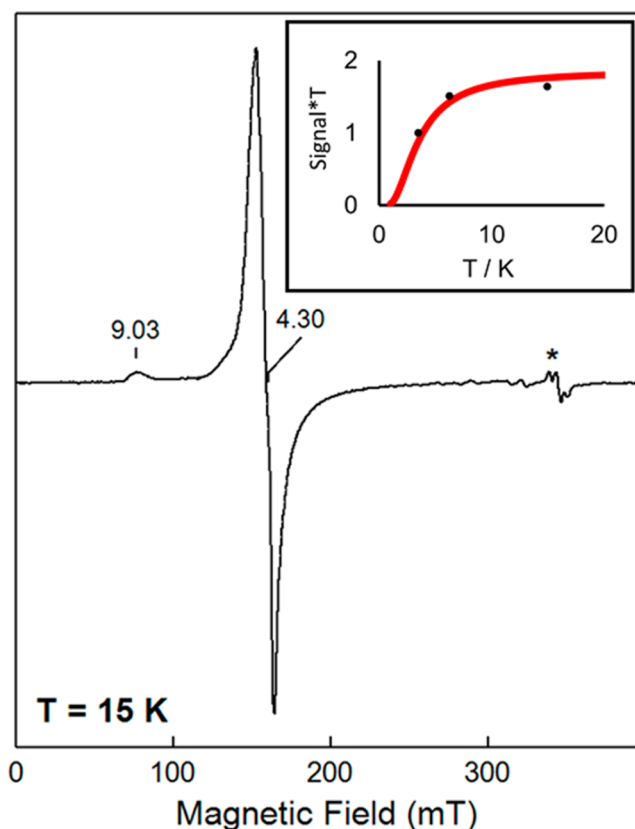


Figure 4. X-band EPR spectrum of a sample containing **3**. The effective g values are indicated. The signal from a minor impurity is labeled as an asterisk. Measurement conditions: microwave frequency, 9.64 GHz; microwave power, $20\text{ }\mu\text{W}$; modulation frequency, 100 kHz; modulation amplitude, 1 mT; measurement temperature, 15 K. (inset) T vs signal $\times T$ plot of $g = 4.3$ EPR resonance recorded at various temperatures (black dots: 4 K, 6 K, 15 K) and fitting curve (red) with $D = 1.1\text{ cm}^{-1}$, $E/D = 0.3$.

magnetic splittings generated from the three Kramers doublets at low field are determined by E/D and the three principal components of the ^{57}Fe hyperfine coupling tensor, A_x , A_y , and A_z . At high field ($>4\text{ T}$), only the ground Kramers doublet is appreciably populated due to the strong magnetic Zeeman interactions; the magnetic splittings are thus largely determined by A_x , A_y , and A_z but independent of E/D . Thus, by simultaneously simulating spectra obtained under low-field and high-field conditions, the full spin-Hamiltonian parameters can be determined reliably and are listed in the caption of Figure 5. (Although a simulation using $D = +1.1\text{ cm}^{-1}$, $\Delta E_Q = -0.85\text{ mm/s}$, and $\eta = 0.3$ is presented in Figure 5, a satisfactory simulation can also be obtained using $D = -1.1\text{ cm}^{-1}$, $\Delta E_Q = +0.85\text{ mm/s}$, and $\eta = 2$.) In addition, the broad line width of the spectra obtained under low-field conditions (Figure 5, top panel) can be best accounted for in a simulation with an E/D distribution of 0.1 centered at $E/D = 0.3$ (see Figure S10c for the simulation without E/D distribution), which is not observed in the spectra measured under high-field conditions due to the insensitivity of those spectral features to E/D . Overall, this $S = 5/2$ species revealed by the Mössbauer measurements accounts for $\sim 85\%$ of the total iron in the sample. The remaining 15% belongs to a minor impurity of unknown origin.

2. Comparison of $[\text{Fe}^{\text{III}}(\text{OH})(\text{TMC-py})]^{2+}$ (3**) with $[(\text{TMC-py})\text{Fe}^{\text{III}}-\text{O}-\text{Cr}^{\text{III}}(\text{OTf})_4(\text{NCMe})]$ (**4**).** To complement the data

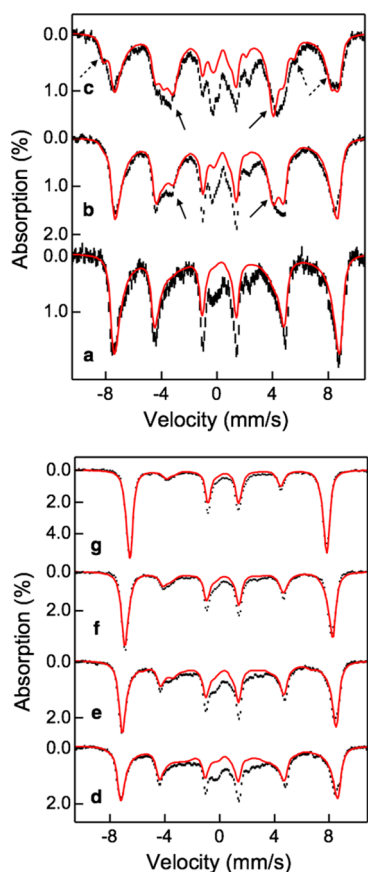


Figure 5. Mössbauer spectra of the sample containing **3** measured under (a) 1.8 K, 45 mT; (b) 4.2 K, 0.1 T; (c) 10 K, 45 mT; (d) 4.2 K, 1.0 T; (e) 4.2 K, 2 T; (f) 4.2 K, 4.0 T; and (g) 4.2 K, 7.0 T. The magnetic fields were applied parallel to the γ -rays. The black vertical bars represent the experimental spectra, and the solid red lines represent the spectral simulation with the parameters of $D = +1.1 \text{ cm}^{-1}$, $E/D = 0.3$, $\sigma(E/D) = 0.1$, $g_x = g_y = g_z = 2$, $\delta = 0.44 \text{ mm/s}$, $\Delta E_Q = -0.85 \text{ mm/s}$, $\eta = 0.3$, $Ax/g_n\beta_n = Ay/g_n\beta_n = Az/g_n\beta_n = -20.7 \text{ T}$. The solid arrows and the dashed arrows indicate the spectral features associated with the middle Kramers doublet and the upper Kramers doublet of the $S = 5/2$ system. The absorption areas that are not covered by the simulations belong to the minor species representing $\sim 15\%$ of the total iron in the sample. These simulations assumed slow relaxation behavior.

we collected thus far on **3**, we also investigated the reaction of **2** with $\text{Cr}(\text{OTf})_2$ to generate the corresponding Fe–O–Cr adduct **4**. As the feasibility of Cr adduct formation was recently demonstrated in the reactions of $\text{Cr}(\text{OTf})_2$ with *syn* or *anti* isomers of the $[\text{Fe}^{\text{IV}}(\text{O})(\text{TMC})]^{2+}$ complex, we thought that **4** would be a suitable complex to compare, as the O–H group in **3** could be replaced by an O–Cr group in **4**.^{22,30} Thus, the $(\text{TMC-py})\text{Fe}^{\text{III}}\text{--O--Cr}^{\text{III}}(\text{OTf})_4(\text{NCMe})$ complex (**4**) was formed at -40°C by the reaction of **2** (0.45 mM solution in MeCN) with 1.25 equiv of $\text{Cr}^{\text{II}}(\text{OTf})_2$ under anaerobic conditions. The characteristic near-IR band of **2** at 834 nm decreased immediately, concomitant with the appearance of new bands at 381, 451, and 558 nm (Figure 6). The latter chromophoric pattern closely resembles that for the $(\text{MeCN})\text{--}(\text{TMC})\text{Fe}^{\text{III}}\text{--O--Cr}^{\text{III}}(\text{OTf})_4(\text{NCMe})$ species.²² Formation of **4** was further supported by the observation of a peak at m/z at 903.8 in its ESI-MS spectrum, which is assigned to the $[(\text{TMC-py})\text{Fe--O--Cr}(\text{OTf})_3]^+$ ion based on its isotope distribution pattern. The formula was further confirmed by an ^{18}O -labeling

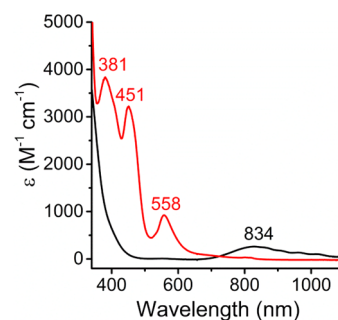


Figure 6. UV-vis spectra of **2** (black) and **4** (red) in MeCN at -40°C .

experiment, which resulted in the upshift of the molecular ion by 2 mass units to m/z 905.8 (see Figures S4 and S5).

The structures of **3** and **4** were further characterized by Fe K-edge XAS. The Fe K-edge energy of **3** is 7124.8 eV, which is a little higher compared with those of **4** (7124.2 eV) and $(\text{MeCN})(\text{TMC})\text{Fe}^{\text{III}}\text{--O}_{\text{anti}}\text{--Cr}^{\text{III}}(\text{OTf})_4(\text{NCMe})$ (7124.0 eV; see Figure 7). Complex **3** exhibits a pre-edge feature at ca. 7114

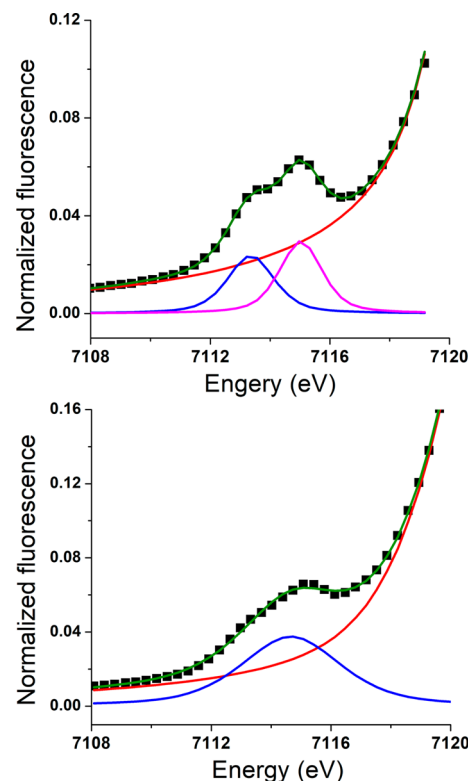


Figure 7. (top) Pre-edge region of the Fe K-edge XAS spectrum of **3** (black squares): rising-edge fit (red line), pre-edge peak 1 (blue line), pre-edge peak 2 (magenta line), pre-edge fit (green line). (bottom) Pre-edge region of the Fe K-edge XAS spectrum of **4** (black squares): rising-edge fit (red line), pre-edge peak 1 (blue line), and pre-edge fit (green line).

eV, which can be fitted with two peaks, providing a combined area of 9.4 units, a value that increases to 14.8 units in **4**. Both pre-edge areas are comparable with that in $(\text{MeCN})(\text{TMC})\text{--Fe}^{\text{III}}\text{--O}_{\text{anti}}\text{--Cr}^{\text{III}}(\text{OTf})_4(\text{NCMe})$ (11 units), but much lower than those in $(\text{TMC})\text{Fe}^{\text{III}}\text{--O}_{\text{syn}}\text{--Cr}^{\text{III}}(\text{OTf})_4(\text{NCMe})$ (30 units)^{22,30} and $(\text{TMC})\text{Fe}^{\text{III}}\text{--O}_{\text{syn}}\text{--Sc}^{\text{III}}(\text{OTf})_4(\text{NCMe})$ (32

units),⁵¹ consistent with the presence of 6-coordinate Fe centers for both 3 and 4.

The XANES data for 3 and 4 are compared with related complexes in Table 1. Interestingly, the table shows that K-edge

Table 1. XANES Data for Iron Complexes of Interest

	K-edge energy (eV)	pre-edge area (units)	ref
[Fe ^{IV} (O)(TMC)(NCMe)] ²⁺	7124.5	32.8	54
[Fe ^{IV} (O)(TMC-Py)] ²⁺ (2)	7124.0	34	29
[Fe ^{III} (OH)(TMC-Py)] ²⁺ (3)	7124.8	9.4	this work
(TMCPy)Fe ^{III} –O–Cr ^{III} (OTf) ₄ (4)	7124.2	14.8	this work
(TMC)Fe ^{III} OCr ^{III} (OTf) ₄	7124.0	11	22
[Fe ^{IV} (O)(OH ₂) ₅] ²⁺	7126	est 70	53
[Fe ^{III} (OH ₂) ₆] ³⁺	7129		53

energies of (TMC)Fe^{IV}(O) and (TMC)Fe^{III}(O–X) complexes are not very different and suggests caution in using *just* K-energies to establish iron oxidation state. This challenge in interpreting K-edge energies has recently been discussed in detail by MacMillan and Lancaster.⁵² In our work, we found the K-edge energies of high-spin ferric centers to span a large range from 7123 to 7129 eV. The highest K-edge energy is associated with the aqueous ferric ion and is 3 eV *higher* than that for the corresponding Fe^{IV}(O) complex.⁵³ In agreement with MacMillan and Lancaster,⁵² we believe that an interpretation of the K-edge energies must also consider the covalency of the iron–ligand bonds. Nevertheless, the oxidation state of the iron center in 3 was unambiguously established by the EPR and Mössbauer data we collected.

Analysis of the EXAFS region provides structural information on the environment of the iron center. The best fit for the EXAFS data of 3 consists of one O/N scatterer at 1.84 Å, five O/N scatterers at 2.17 Å, four C scatterers at 2.92 Å, and four C scatterers at 3.07 Å (Figure 8, top; Table S1). Remarkably, 4 gives nearly identical results for the first coordination sphere with one O/N scatterer at 1.84 Å and five O/N scatterers at 2.16 Å (Figure 8, bottom; Table S2), but the outer sphere differs in having a strong contribution from a Cr scatterer at 3.65 Å. The Fe^{III}–O/N bond distances of both 3 and 4 also fall in the range of the bond distances in other iron(III) complexes of TMC-based supporting ligands (see Table 2). Moreover, the Fe(III)–O(H) and Fe(III)–N_{ave} bond distances in 3 agree with values found in the crystal structure of the high-spin Fe^{III}(tnpa)(OH)(PhCOO)(ClO₄) complex.¹¹ In conclusion, the XAS data indicate the presence of 6-coordinate Fe(III) centers in both 3 and 4.

3. Density Functional Theory Calculations. We next set out to compare the Fe^{III}–OH bond distance obtained from EXAFS measurements with values predicted from density functional theory (DFT) calculations. For these calculations we considered two conformations of the TMC macrocycle derived from the X-ray crystal structures of [Fe^{IV}(O)(TMC-py)]²⁺, which has the two opposed N–CH₂–CH₂–N linkages oriented in a “parallel” fashion, and that of [Fe^{II}(TMC-py)]²⁺, which has these linkages oriented in a “crossed” fashion.¹⁶ At the M06-L/def2-SVP(Fe: def2-TZVP)/COSMO(MeCN) level of theory for the *S* = 5/2 spin state, we obtained Fe–OH bond distances of 1.837 and 1.850 Å for the [Fe^{III}(OH)(TMC-py)]²⁺ complex with parallel and crossed conformations, respectively (Figure

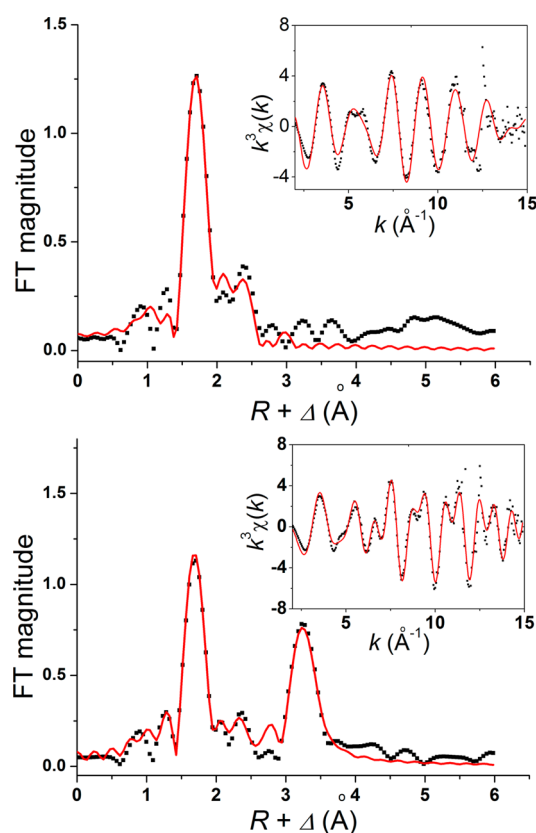


Figure 8. (top) Fourier-transformed Fe K-edge EXAFS data for 3 (dotted black) and the corresponding best fit (solid red, fit No. 6 in Table S1). (inset) Unfiltered *k*-space data (dotted black) and its fit (solid red). (bottom) Fourier-transformed Fe K-edge EXAFS data for 4 (dotted black) and the corresponding best fit (solid red, fit No. 6 in Table S2). (inset) Unfiltered *k*-space data (dotted black) and its fit (solid red).

9), and we found the parallel conformation to be energetically slightly favored ($\Delta G_{233} = 2.7$ kcal mol^{−1}). These bond distances are in quantitative agreement with the experimental value of 1.84 Å as determined by EXAFS measurements. Single-point calculations at these geometries using the M06-L and M06 functionals in combination with the more complete def2-TZVPP basis set and COSMO(MeCN) predict the energetic difference between these conformers to be 2.6 and 3.0 kcal mol^{−1} (ΔG_{233}), respectively. We also investigated intermediate (*S* = 3/2) and low (*S* = 1/2) spin states using the M06-L functional, which we recently demonstrated to be suitable for the determination of the spin ground state.⁵⁷ We found these to be energetically less favorable and to provide poorer agreement with the experimentally determined Fe–OH bond distance (see Supporting Information Table S3).

4. Reactivity of Fe^{III}(OH)(TMC-py)(OTf)₂ (3) with TEMPOH. [Fe^{III}(OH)(TMC-py)](OTf)₂ (3) is generated from 2 by reaction with excess CHD at −40 °C but is not a powerful enough oxidant to react further with excess CHD (bond dissociation energy (BDE) \approx 77 kcal mol^{−1}) indicating that the generated Fe^{III}–OH complex 3 is only poorly reactive. This is in contrast to related Fe^{III} complexes bearing the Py5 ligand (Py5 = (2,6-bis(bis(2-pyridyl)methoxymethane)-pyridine), which are capable of breaking relatively strong C–H bonds and readily oxidize CHD.^{58,59}

However, 3 does decay at −40 °C over the course of 1 h, suggesting that it has the potential to react further. On the basis

Table 2. Select Bond Distances of Iron(III)–OX Complexes

complexes ^a	Fe–O ^b	Fe–N _{ave} ^b	spin state ^c	ref
soybean lipoxygenase	1.88	2.12	5/2	55
[Fe ^{III} (OH)(TMC-py)](OTf) ₂ (3)	1.84	2.17	5/2	<i>d</i>
(TMC-py)Fe ^{III} –O–Cr ^{III} (OTf) ₄ (NCMe) (4)	1.84	2.16	1	<i>d</i>
(Me ₃ cyclam-acetate)Fe ^{III} –O–Fe ^{III} Cl ₃	1.802(2)	2.174	0	56
(Cl)(TMC)Fe ^{III} –O _{anti} –Fe ^{III} Cl ₃	1.8510(12)	2.206	0	30
(MeCN)(TMC)Fe ^{III} –O _{anti} –Cr ^{III} (OTf) ₄ (NCMe)	1.81	2.17	1	22
(NCS)(TMC)Fe ^{III} –O _{anti} –Cr ^{III} (OTf) ₄ (NCMe)	1.85	2.17	1	22
Fe ^{III} (OH)(tnpa)(O ₂ CPh)(ClO ₄)	1.876(2)	2.188	5/2	11
[Fe ^{III} (OH)(TMG ₃ tren)](OTf) ₂	1.77	2.000	5/2	14
K[Fe ^{III} (OH)(H ₃ buea)]	1.9264(17)	2.016	5/2	13

^aAbbreviations used: H₃buea = 1,1,1-tris[(*N*-*tert*-butylureaylato)-*N*-ethyl]aminato trianion; Me₃cyclam-acetate = 1-(carboxymethyl)-4,8,11-trimethyl-1,4,8,11-tetrazacyclotetradecane anion; TMG₃tren = 1,1,1-tris{2-[N2-(1,1,3,3-tetramethylguanidino)]ethyl}amine; tnpa = tris(6-neopentylamino-2-pyridylmethyl)amine). ^bBond distances from EXAFS analysis have uncertainties of ± 0.02 Å, while those with higher precision derive from XRD. ^cSpin states listed for dinuclear complexes refer to the entire complex; individual iron(III) centers are all high-spin. ^dThis work.

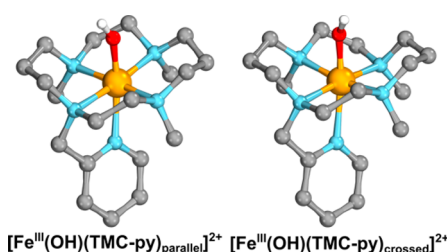
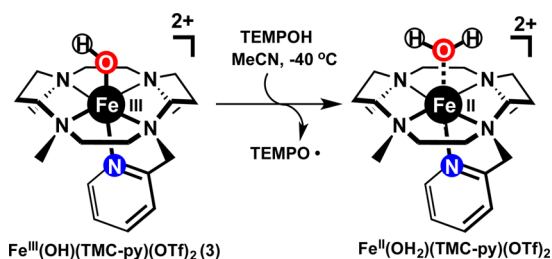


Figure 9. Structural depictions of the crossed and parallel conformations of [Fe^{III}(OH)(TMC-py)]²⁺ at the M06-L/def2-SVP-(Fe: def2-TZVP)/COSMO(MeCN) level of theory for the *S* = 5/2 spin state.

of the premise that 3 may be able to react with organic substrates having weaker X–H bonds, such as TEMPOH ($D_{\text{O–H}} \approx 70$ kcal/mol; Scheme 2),^{60,61} 40 equiv of TEMPOH

Scheme 2. Reaction of Fe^{III}(OH)(TMC-py)(OTf)₂ (3) with TEMPOH



were added to a solution of 3, and the latter decayed completely within 1 min (Figure 10, top). A TEMPOH concentration dependence study afforded a k_2 value of $7.1 \text{ M}^{-1} \text{ s}^{-1}$, which decreased sixfold to $1.2 \text{ M}^{-1} \text{ s}^{-1}$, when TEMPOD was used in place of TEMPOH (Figure 10, bottom). Analysis of the product solution by ESI-MS showed that [Fe^{II}(TMC-py)(OTf)]⁺ was formed as the major product, while EPR analysis revealed the formation of TEMPO radical in nearly quantitative yield (93%). Notably, the KIE value for TEMPOH/D oxidation by 3 is higher than those reported in the literature for O–H bond cleavage reactions by other Fe^{III}–OH and Mn^{III}–OH complexes (see Table 3). In addition, no reaction was observed at -40 °C for other potential substrates such as 2,4,6-tri-*tert*-butylphenol (O–H BDE ≈ 81 kcal/mol) and xanthene (C–H BDE ≈ 75.5 kcal/mol).^{61,62}

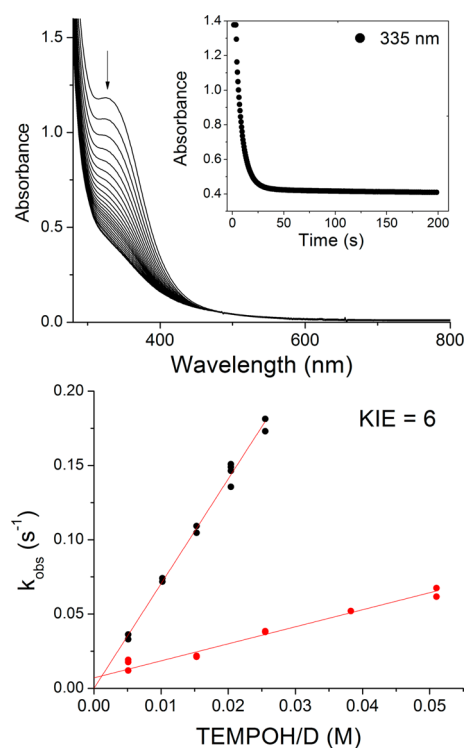


Figure 10. (top) UV–vis spectral changes upon addition of 40 equiv of TEMPOH into a solution of Fe^{III}(OH)(TMC-py)(OTf)₂ (3) in MeCN at -40 °C. (bottom) k_2 plots for the reactions of 3 with varying amounts of TEMPOH (black ●) and TEMPOD (red ●) at -40 °C.

The observed KIE of 6 for the reaction of 3 with TEMPOH at -40 °C is larger than all reactions listed in Table 3, except for the two cases involving C–H bond cleavage. This raises the question of whether the reaction mechanism involves HAT, where the proton and the electron both originate from the O–H bond and travel together to the same location, or a proton-coupled electron transfer (PCET), where the origin and destination of the proton and the electron transferred do not have to coincide, and thus both entities travel separately. We note here that the nomenclature for such processes is not always consistent in the literature. For the sake of simplicity we use the definition outlined above, which was also used by Usharani et al.⁶⁷ (For more detailed definitions of different reaction scenarios associated with PCET reactions, see refs

Table 3. Second-Order Rate Constants for $M^{III}-O(H/Me)$ Species Reactions with TEMPOH

complexes ^a	k_2 ($M^{-1} s^{-1}$, 25 °C)	KIE	ref
$[Fe^{III}(OH)(TMC-py)]^{2+}$ (3)	7.1 (−40 °C)	6 (−40 °C)	<i>b</i>
$[Fe^{III}(OH)(PYS)]^{2+}$	$4.3(3) \times 10^{-4}$	6.3 (DHA)	59
$[Fe^{III}(OMe)(PYS)]^{2+}$	$6.0(5) \times 10^{-1}$	2.0 (⁴⁺ -BuArOH)	58
$[Fe^{III}(OH)(TMP)]$	$7.6(5) \times 10^1$		63
$[Fe^{III}(OH)(OH_2)(PyPz)]^{4+}$	2216(28) (20 °C)	20.2(3) (xanthene)	62
$[Mn^{III}(OH)(dpaq^H)]^{1+}$	$1.3(1) \times 10^{-1}$	1.8	61
$[Mn^{III}(OMe)(dpaq^H)]^{1+}$	$8.0(1) \times 10^{-2}$	1.8	64
$[Mn^{III}(OH)(dpaq^{2Me})]^{1+}$	$3.9(3) (-35\text{ °C})$	$2.7 (-35\text{ °C})$	65
$[Mn^{III}(OH)(S^{Me_2}N_4(tren))]^{1+}$	2.1×10^3	3.1	66
$[Mn^{III}(OMe)(S^{Me_2}N_4(tren))]^{1+}$	3.6×10^2	2.1	66

^aAbbreviations used: $dpaq^H = 2$ -[bis(pyridin-2-ylmethyl)]amino-*N*-quinolin-8-yl-acetamidate anion; $dpaq^{2Me} = 2$ -[bis(pyridin-2-ylmethyl)]amino-*N*-2-methyl-quinolin-8-yl-acetamidate anion; ^ePy5 = (2,6-bis(bis(2-pyridyl)methoxymethane)pyridine; PyPz = quaternized tetra-2,3-pyridinoporphyrazine; $S^{Me_2}N_4(tren) = 3'$ -mercapto-3',3'-dimethyl-2'-propylimino-tris(2-aminoethyl)amine; TMP = *meso*-tetramesitylporphyrinate. ^bThis work.

68–70.) From the second-order rate constant of $7.1\text{ M}^{-1}\text{ s}^{-1}$, we calculate an apparent free energy of activation of $12.6\text{ kcal mol}^{-1}$ as described in ref 71. To clarify the aspect outlined above, we optimized the reaction path at the M06-L/def2-SVP(Fe:def2-TZVP)/COSMO(MeCN) level of theory for the $S = 5/2$ spin state followed by single-point energy calculations at the M06-L/def2-TZVP/COSMO(MeCN) and M06/def2-TZVP/COSMO(MeCN) levels of theory. In the following, we will only refer to the given functional name reflecting the above outlined methodology. We again considered parallel and crossed conformations of the macrocycle. In Figure 11 Lewis structures of the studied path are depicted (for structural depictions see Figure S11). Computed free energies are shown in Table 4.

We obtained barriers of 8.7 and $10.4\text{ kcal mol}^{-1}$ for the parallel and crossed conformations. These values somewhat

Table 4. Computed Free Energies^a (ΔG_{233} in kcal mol^{-1}) for the Reaction between TEMPOH and $[Fe^{III}(OH)(TMC-py)]^{2+}$

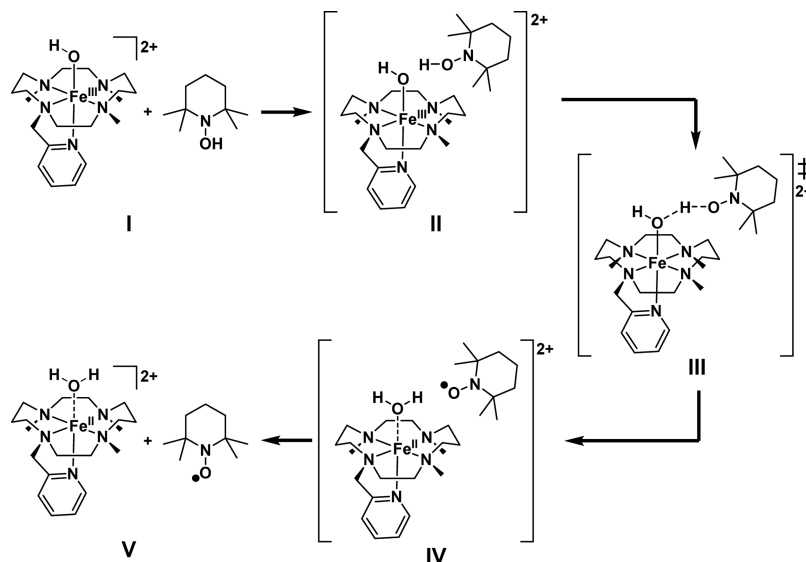
structure	I	II	III	IV	V
M06-L	0.0 [2.6]	3.5 [7.3]	8.7 [10.4]	0.6 [1.5]	−2.7 [−5.3]
M06	0.0 [3.0]	5.0 [9.2]	13.6 [16.2]	−3.7 [−3.1]	−8.2 [−12.2]

^aElectronic energies were computed with the indicated functional using the def2-TZVPP basis set and COSMO(MeCN) on M06-L/def2-SVP(Fe:def2-TZVP)/COSMO(MeCN) geometries. Values refer to the “parallel” conformation, and values in brackets refer to the “crossed” conformation.

underestimate the experimentally observed values, which one might attribute to the local functional nature of M06-L. Computing energies with the hybrid functional M06 results in the prediction of slightly higher barriers of 13.6 and $16.2\text{ kcal mol}^{-1}$ for the parallel and crossed conformers (Table 4), which agree very well with the experimentally determined value of $12.6\text{ kcal mol}^{-1}$. We do note that we did not include any tunneling contribution, which would result in a reduction of the apparent barrier height.

One item we observe is that, once the +II oxidation state is reached, the crossed conformation becomes energetically favored, independent of the functional chosen. Furthermore, the $Fe^{II}-OH_2$ distances in the resulting $[Fe^{II}(OH_2)(TMC-py)]^{2+}$ complexes with parallel and crossed conformations are rather long at 2.423 and 3.332 Å , respectively. We note that all Fe^{II} complexes supported by the TMC framework crystallographically characterized thus far are all five-coordinate and have a conformation consistent with our definition of crossed.^{16,29,72–76}

To address the initially posed question of whether this reaction proceeds via HAT or PCET, we analyzed the changes in localized orbitals, more specifically, the intrinsic bond orbitals (IBOs),⁴⁸ for intermediates II, III, and IV. It was previously demonstrated that this formalism can be used to analyze the electron flow of a given reaction.⁴⁹ Notably, here we apply this methodology to an open-shell system for the first time. For this purpose, we treat α and β electrons separately, leading to two independent sets of localized orbitals. Consistent

**Figure 11.** Lewis structure depictions of the studied reaction pathway.

with the experimentally determined spin state of $S = 5/2$ for the $\text{Fe}^{\text{III}}\text{--OH}$ complex, we can identify five singly occupied d-orbitals in the α -spin manifold with no β counterparts on Fe for structure **II**. These are shown in Figure S12. As the Fe^{III} center is reduced to Fe^{II} , one of the d-orbitals becomes occupied by a β electron derived from TEMPOH, leading to an $S = 2$ spin state on the reduced Fe^{II} center in **IV**. This leaves an α electron behind on the TEMPO radical that is ferromagnetically coupled to the Fe^{II} center (see spin density plot in Figure S13 and spin populations in Table S4). This scenario differs from the one described for the reaction between TEMPOH and a $\text{Mn}^{\text{III}}\text{--OH}$ complex, where an α electron is transferred, leading to an anti-ferromagnetic coupling of the resulting radical on TEMPO and the $\text{Mn}^{\text{II}}\text{--OH}_2$ site.⁶⁵ In the reaction of the $\text{Fe}^{\text{III}}\text{--OH}$ complex, we only need to inspect the changes that occur in the β spin manifold to identify which electron has been transferred from TEMPOH to the $\text{Fe}^{\text{III}}\text{--OH}$ complex. To be more specific, if the β electron transfers out of the O–H bond of TEMPOH and travels together with the proton in the form of a hydrogen radical, the reaction path would be classified as HAT. In contrast to this scenario, the transfer of an electron originating from some other orbital of TEMPOH to Fe^{III} would more properly be described as a PCET. For a related analysis employing canonical orbital picture see ref 77.

In Figure 12 (top) we show the changes to the β electron of the O–H bond of the TEMPOH molecule. In the trans-

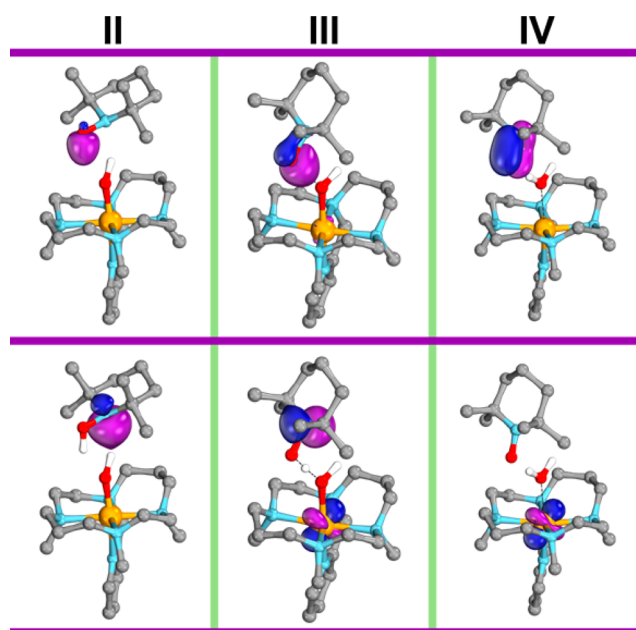


Figure 12. Changes of the intrinsic bond orbitals associated with the β electrons of the O–H bond (top) and N lone pair (bottom) at the M06-L/def2-TZVPP/COSMO(MeCN) level of theory at M06-L/def2-SVP(Fe: def2-TZVP)/COSMO(MeCN) geometries.

formation from **II** to **IV** the electron associated with this localized orbital (IBO) is not transferred to the $\text{Fe}^{\text{III}}\text{--OH}$ complex. Instead, the changes to this IBO are modest in the TS structure **III**. After reduction of the Fe^{III} center to Fe^{II} and generation of the TEMPO radical, the IBO becomes delocalized and is part of a π -bonding interaction between oxygen and nitrogen in structure **IV**. Further inspection of the IBOs associated with the TEMPOH molecule reveals that it is the β electron from the lone pair of the N atom that is

transferred to the iron center, as shown in Figure 12 (bottom). This becomes particularly clear in the TS structure **III** and is consistent with the observed behavior of the β electron initially associated with the O–H bond of the TEMPOH molecule; that is, as the β electron is transferred from the N lone pair to the Fe center, a hole is generated, which is positioned such that in structure **IV** the β electron from the former O–H bond delocalizes as shown in Figure 12 (top). In this process, the proton is transferred to a lone pair on the $\text{Fe}^{\text{III}}\text{--OH}$ group. The IBO changes associated with the proton transfer are shown in Figure S14. As such, the proton transfer reaction resembles an acid/base reaction. Notably, acid/base reactions can exhibit nonclassical KIEs associated with proton transfer.^{78,79}

We compared our IBO-based results with respect to the HAT versus PCET nature of this reaction to an analysis of deformation energies proposed by Usharani et al.⁶⁷ With the latter approach, we again obtain results more consistent with a PCET scenario (see Table S4). We therefore assign the reaction of our $\text{Fe}^{\text{III}}\text{--OH}$ complex with TEMPOH, to be PCET in nature. This reaction may thus be regarded as a model for the reactivity of soybean lipoxygenase, which has similarly been proposed to react with weak C–H bonds via PCET.^{80–88}

CONCLUSIONS

To date, there are only two crystallographically characterized $\text{Fe}^{\text{III}}\text{--OH}$ complexes in nonheme ligand environments; in both examples, the $\text{Fe}^{\text{III}}\text{--OH}$ units are stabilized by hydrogen bonding groups designed into the supporting ligands.^{11,13} Here, we successfully characterized the thermally unstable high-spin $\text{Fe}^{\text{III}}(\text{OH})(\text{TMC-py})(\text{OTf})_2$ (**3**) complex using UV–vis, EPR, EXAFS, and Mössbauer spectroscopies and ESI-MS. Structural parameters obtained from EXAFS measurements were supported computationally. The results not only shed new light into structural and electronic features of intermediates of this type but also provide evidence that the reaction of $\text{Fe}^{\text{IV}}(\text{O})(\text{TMC-py})(\text{OTf})_2$ with CHD forms an $\text{Fe}(\text{III})\text{--OH}$ complex as the initial product. Insight into the reactivity of such poorly understood iron(III)–hydroxide complexes has been obtained by studying the reaction of **3** with TEMPOH both experimentally and computationally. On the basis of computational analysis we classify the reaction as having PCET-like character, consistent with the proposed reaction channel for the $\text{Fe}^{\text{III}}\text{--OH}$ oxidant associated with soybean lipoxygenase.^{80–88}

ASSOCIATED CONTENT

Supporting Information

The Supporting Information is available free of charge on the ACS Publications website at DOI: 10.1021/acs.inorgchem.7b01459.

Additional information on EXAFS analysis for complexes **3** and **4**; NMR data for **1** and **2**; mass spectrometric data for **4**; EPR and Mössbauer data for **3**; additional computational details and Cartesian coordinates (PDF)

AUTHOR INFORMATION

Corresponding Authors

*E-mail: cramer@umn.edu. Twitter: @ChemProfCramer. (C.J.C.)

*E-mail: ysguo@andrew.cmu.edu. (Y.G.)

*E-mail: larryque@umn.edu. (L.Q.)

ORCID

Wei-Min Ching: 0000-0002-5299-4479

Johannes E. M. N. Klein: 0000-0002-1290-597X

Gerald Knizia: 0000-0002-7163-4823

Christopher J. Cramer: 0000-0001-5048-1859

Yisong Guo: 0000-0002-4132-3565

Lawrence Que Jr.: 0000-0002-0989-2813

Present Address

[†]Instrumentation Center, Department of Chemistry, National Taiwan Normal University, Taipei 11677, Taiwan.

Notes

The authors declare no competing financial interest.

■ ACKNOWLEDGMENTS

This work was supported by the U.S. National Science Foundation (Grant Nos. CHE-1361773 to L.Q., CHE-1361595 to C.J.C., and CHE-1654060 to Y.G.) and the U.S. National Institutes of Health (Grant No. GM38767 to L.Q.). W.-M.C. acknowledges the Ministry of Science and Technology, Taiwan, for a postdoctoral fellowship, and J.E.M.N.K. thanks the Alexander von Humboldt Foundation for a Feodor Lynen Research Fellowship. XAS data were collected on Beamlines 7-3 and 9-3 at the Stanford Synchrotron Radiation Lightsource, SLAC National Accelerator Laboratory, which is supported by the U.S. Department of Energy (DOE), Office of Science, Office of Basic Energy Sciences under Contract No. DE-AC02-76SF00515. Use of Beamlines 7-3 and 9-3 is supported by the DOE Office of Biological and Environmental Research, and by the National Institutes of Health, National Institute of General Medical Sciences (including P41GM103393). The authors acknowledge the Minnesota Supercomputing Institute (MSI) at the University of Minnesota for providing resources that contributed to the research results reported within this paper. R.F. and Y.G. also thank Prof. M. Hendrich for his assistance with the EPR instrument.

■ REFERENCES

- (1) Price, J. C.; Barr, E. W.; Tirupati, B.; Bollinger, J. M., Jr.; Krebs, C. The First Direct Characterization of a High-Valent Iron Intermediate in the Reaction of an α -Ketoglutarate-Dependent Dioxygenase: A High-Spin Fe(IV) Complex in Taurine/ α -Ketoglutarate Dioxygenase (TauD) from *Escherichia coli*. *Biochemistry* **2003**, *42*, 7497–7508.
- (2) Bollinger, J. M.; Krebs, C. Stalking intermediates in oxygen activation by iron enzymes: Motivation and method. *J. Inorg. Biochem.* **2006**, *100*, 586–605.
- (3) Krebs, C.; Galonić Fujimori, D.; Walsh, C. T.; Bollinger, J. M., Jr. Non-Heme Fe(IV)-Oxo Intermediates. *Acc. Chem. Res.* **2007**, *40*, 484–492.
- (4) Bollinger, J. M.; Price, J. C.; Hoffart, L. M.; Barr, E. W.; Krebs, C. Mechanism of Taurine: α -Ketoglutarate Dioxygenase (TauD) from *Escherichia coli*. *Eur. J. Inorg. Chem.* **2005**, *2005*, 4245–4254.
- (5) Rohde, J.-U.; In, J.-H.; Lim, M. H.; Brennessel, W. W.; Bukowski, M. R.; Stubna, A.; Münck, E.; Nam, W.; Que, L., Jr. Crystallographic and Spectroscopic Characterization of a Nonheme Fe(IV)=O Complex. *Science* **2003**, *299*, 1037–1039.
- (6) Klein, J. E. M. N.; Que, L., Jr. *Biomimetic High-Valent Mononuclear Nonheme Iron-Oxo Chemistry in Encyclopedia of Inorganic and Bioinorganic Chemistry (EIBC)*; John Wiley & Sons, Ltd, 2016, DOI: 10.1002/9781119951438.eibc2344.
- (7) McDonald, A. R.; Que, L., Jr. High-valent nonheme iron-oxo complexes: Synthesis, structure, and spectroscopy. *Coord. Chem. Rev.* **2013**, *257*, 414–428.
- (8) Ray, K.; Pfaff, F. F.; Wang, B.; Nam, W. Status of Reactive Non-Heme Metal–Oxygen Intermediates in Chemical and Enzymatic Reactions. *J. Am. Chem. Soc.* **2014**, *136*, 13942–13958.
- (9) Puri, M.; Que, L., Jr. Toward the Synthesis of More Reactive S = 2 Non-Heme Oxoiron(IV) Complexes. *Acc. Chem. Res.* **2015**, *48*, 2443–2452.
- (10) Sastri, C. V.; Lee, J.; Oh, K.; Lee, Y. J.; Lee, J.; Jackson, T. A.; Ray, K.; Hirao, H.; Shin, W.; Halfen, J. A.; Kim, J.; Que, L., Jr.; Shaik, S.; Nam, W. Axial ligand tuning of a nonheme iron(IV)–oxo unit for hydrogen atom abstraction. *Proc. Natl. Acad. Sci. U. S. A.* **2007**, *104*, 19181–19186.
- (11) Ogo, S.; Wada, S.; Watanabe, Y.; Iwase, M.; Wada, A.; Harata, M.; Jitsukawa, K.; Masuda, H.; Einaga, H. Synthesis, Structure, and Spectroscopic Properties of $[\text{Fe}^{\text{III}}(\text{tnpa})(\text{OH})(\text{PhCOO})]\text{ClO}_4$: A Model Complex for an Active Form of Soybean Lipooxygenase-1. *Angew. Chem., Int. Ed.* **1998**, *37*, 2102–2104.
- (12) MacBeth, C. E.; Golombek, A. P.; Young, V. G.; Yang, C.; Kuczera, K.; Hendrich, M. P.; Borovik, A. S. O₂ Activation by Nonheme Iron Complexes: A Monomeric Fe(III)-oxo Complex Derived from O₂. *Science* **2000**, *289*, 938–941.
- (13) MacBeth, C. E.; Gupta, R.; Mitchell-Koch, K. R.; Young, V. G.; Lushington, G. H.; Thompson, W. H.; Hendrich, M. P.; Borovik, A. S. Utilization of Hydrogen Bonds To Stabilize M–O(H) Units: Synthesis and Properties of Monomeric Iron and Manganese Complexes with Terminal Oxo and Hydroxo Ligands. *J. Am. Chem. Soc.* **2004**, *126*, 2556–2567.
- (14) England, J.; Guo, Y.; Farquhar, E. R.; Young, V. G., Jr.; Münck, E.; Que, L., Jr. The Crystal Structure of a High-Spin Oxoiron(IV) Complex and Characterization of Its Self-Decay Pathway. *J. Am. Chem. Soc.* **2010**, *132*, 8635–8644.
- (15) Prakash, J.; Rohde, G. T.; Meier, K. K.; Münck, E.; Que, L., Jr. Upside Down! Crystallographic and Spectroscopic Characterization of an $[\text{Fe}^{\text{IV}}(\text{O}_{\text{syn}})(\text{TMC})]^{2+}$ Complex. *Inorg. Chem.* **2015**, *54*, 11055–11057.
- (16) Thibon, A.; England, J.; Martinho, M.; Young, V. G., Jr.; Frisch, J. R.; Guillot, R.; Girerd, J.-J.; Münck, E.; Que, L., Jr.; Banse, F. Proton- and Reductant-Assisted Dioxygen Activation by a Nonheme Iron(II) Complex to Form an Oxoiron(IV) Intermediate. *Angew. Chem., Int. Ed.* **2008**, *47*, 7064–7067.
- (17) Lee, Y.-M.; Kotani, H.; Suenobu, T.; Nam, W.; Fukuzumi, S. Fundamental Electron-Transfer Properties of Non-heme Oxoiron(IV) Complexes. *J. Am. Chem. Soc.* **2008**, *130*, 434–435.
- (18) Fukuzumi, S.; Kotani, H.; Suenobu, T.; Hong, S.; Lee, Y.-M.; Nam, W. Contrasting Effects of Axial Ligands on Electron-Transfer Versus Proton-Coupled Electron-Transfer Reactions of Nonheme Oxoiron(IV) Complexes. *Chem. - Eur. J.* **2010**, *16*, 354–361.
- (19) Matson, E. M.; Park, Y. J.; Fout, A. R. Facile Nitrite Reduction in a Non-heme Iron System: Formation of an Iron(III)-Oxo. *J. Am. Chem. Soc.* **2014**, *136*, 17398–17401.
- (20) Armarego, W. L. F.; Chai, C. *Chapter 4 - Purification of Organic Chemicals. In Purification of Laboratory Chemicals*, 7th ed.; Butterworth-Heinemann: Boston, MA, 2013; pp 103–554.
- (21) Hagadorn, J. R.; Que, L., Jr.; Tolman, W. B. N-Donor Effects on Carboxylate Binding in Mononuclear Iron(II) Complexes of a Sterically Hindered Benzoate Ligand. *Inorg. Chem.* **2000**, *39*, 6086–6090.
- (22) Zhou, A.; Kleespies, S. T.; Van Heuvelen, K. M.; Que, L., Jr. Characterization of a heterobimetallic nonheme Fe(III)-O-Cr(III) species formed by O₂ activation. *Chem. Commun.* **2015**, *51*, 14326–14329.
- (23) Mader, E. A.; Davidson, E. R.; Mayer, J. M. Large Ground-State Entropy Changes for Hydrogen Atom Transfer Reactions of Iron Complexes. *J. Am. Chem. Soc.* **2007**, *129*, 5153–5166.
- (24) Wu, A.; Mader, E. A.; Datta, A.; Hrovat, D. A.; Borden, W. T.; Mayer, J. M. Nitroxyl Radical Plus Hydroxylamine Pseudo Self-Exchange Reactions: Tunneling in Hydrogen Atom Transfer. *J. Am. Chem. Soc.* **2009**, *131*, 11985–11997.
- (25) Havare, N.; Plattner, D. A. Oxidative Cleavage of α -Aryl Aldehydes Using Iodosylbenzene. *Org. Lett.* **2012**, *14*, 5078–5081.
- (26) Petasis, D. T.; Hendrich, M. P. Chapter Eight-Quantitative Interpretation of Multifrequency Multimode EPR Spectra of Metal

Containing Proteins, Enzymes, and Biomimetic Complexes. *Methods Enzymol.* **2015**, 563, 171–208.

(27) George, G. N. *EXAFSPAK*, Stanford Synchrotron Radiation Laboratory; Stanford Linear Accelerator Center: Stanford, CA, 2000.

(28) Wojdyr, M. *Fityk*: a general-purpose peak fitting program. *J. Appl. Crystallogr.* **2010**, 43, 1126–1128.

(29) England, J.; Bigelow, J. O.; Van Heuvelen, K. M.; Farquhar, E. R.; Martinho, M.; Meier, K. K.; Frisch, J. R.; Münck, E.; Que, L., Jr. An ultra-stable oxoiron(IV) complex and its blue conjugate base. *Chem. Sci.* **2014**, 5, 1204–1215.

(30) Zhou, A.; Prakash, J.; Rohde, G. T.; Klein, J. E. M. N.; Kleespies, S. T.; Draksharapu, A.; Fan, R.; Guo, Y.; Cramer, C. J.; Que, L., Jr. The Two Faces of Tetramethylcyclam in Iron Chemistry: Distinct Fe–O–M Complexes Derived from $[\text{Fe}^{\text{IV}}(\text{O}_{\text{anti/syn}})(\text{TMC})]^{2+}$ Isomers. *Inorg. Chem.* **2017**, 56, 518–527.

(31) Ahlrichs, R.; Bär, M.; Häser, M.; Horn, H.; Kölmel, C. Electronic structure calculations on workstation computers: The program system turbomole. *Chem. Phys. Lett.* **1989**, 162, 165–169.

(32) Furche, F.; Ahlrichs, R.; Hättig, C.; Klopper, W.; Sierka, M.; Weigend, F. Turbomole. *WIREs Comput. Mol. Sci.* **2014**, 4, 91–100.

(33) *TURBOMOLE*, V7.0.1 2015, a development of University of Karlsruhe and Forschungszentrum Karlsruhe GmbH, 1989–2007; *TURBOMOLE* GmbH, since 2007; available from <http://www.turbomole.com>.

(34) Zhao, Y.; Truhlar, D. G. A new local density functional for main-group thermochemistry, transition metal bonding, thermochemical kinetics, and noncovalent interactions. *J. Chem. Phys.* **2006**, 125, 194101.

(35) Weigend, F.; Ahlrichs, R. Balanced basis sets of split valence, triple zeta valence and quadruple zeta valence quality for H to Rn: Design and assessment of accuracy. *Phys. Chem. Chem. Phys.* **2005**, 7, 3297–3305.

(36) Zhao, Y.; Truhlar, D. The M06 suite of density functionals for main group thermochemistry, thermochemical kinetics, noncovalent interactions, excited states, and transition elements: two new functionals and systematic testing of four M06-class functionals and 12 other functionals. *Theor. Chem. Acc.* **2008**, 120, 215–241.

(37) Gagliardi, L. G.; Castells, C. B.; Ràfols, C.; Rosés, M.; Bosch, E. Static Dielectric Constants of Acetonitrile/Water Mixtures at Different Temperatures and Debye–Hückel A and a_0B Parameters for Activity Coefficients. *J. Chem. Eng. Data* **2007**, 52, 1103–1107.

(38) Lowry, T. M.; Henderson, S. T. Molecular Structure and Physical Properties of Prussic Acid. Part I. Refractive Dispersion of Prussic Acid and Its Homologues. *Proc. R. Soc. London, Ser. A* **1932**, 136, 471–487.

(39) <http://www.sigmaaldrich.com/chemistry/solvents/acetonitrile-center.html> Accessed June 7, 2016.

(40) Klamt, A.; Schüürmann, G. COSMO: A New Approach to Dielectric Screening in Solvents with Explicit Expressions for the Screening Energy and its Gradient. *J. Chem. Soc., Perkin Trans. 2* **1993**, 2, 799–805.

(41) Klamt, A.; Jonas, V. Treatment of the outlying charge in continuum solvation models. *J. Chem. Phys.* **1996**, 105, 9972–9981.

(42) Averkiev, B. B.; Truhlar, D. G. Free energy of reaction by density functional theory: oxidative addition of ammonia by an iridium complex with PCP pincer ligands. *Catal. Sci. Technol.* **2011**, 1, 1526–1529.

(43) Ribeiro, R. F.; Marenich, A. V.; Cramer, C. J.; Truhlar, D. G. Use of Solution-Phase Vibrational Frequencies in Continuum Models for the Free Energy of Solvation. *J. Phys. Chem. B* **2011**, 115, 14556–14562.

(44) Bryantsev, V. S.; Diallo, M. S.; Goddard, W. A., III Calculation of Solvation Free Energies of Charged Solutes Using Mixed Cluster/Continuum Models. *J. Phys. Chem. B* **2008**, 112, 9709–9719.

(45) Sierka, M.; Hoge Kamp, A.; Ahlrichs, R. Fast evaluation of the Coulomb potential for electron densities using multipole accelerated resolution of identity approximation. *J. Chem. Phys.* **2003**, 118, 9136–9148.

(46) Weigend, F. Accurate Coulomb-fitting basis sets for H to Rn. *Phys. Chem. Chem. Phys.* **2006**, 8, 1057–1065.

(47) Hellweg, A. Heuristic control of kinetic energy in dynamic reaction coordinate calculations. *J. Comput. Chem.* **2013**, 34, 1835–1841.

(48) Knizia, G. Intrinsic Atomic Orbitals: An Unbiased Bridge between Quantum Theory and Chemical Concepts. *J. Chem. Theory Comput.* **2013**, 9, 4834–4843.

(49) Knizia, G.; Klein, J. E. M. N. Electron Flow in Reaction Mechanisms—Revealed from First Principles. *Angew. Chem., Int. Ed.* **2015**, 54, 5518–5522.

(50) Knizia, G. <http://www.iboview.org/>.

(51) Prakash, J.; Rohde, G. T.; Meier, K. K.; Jasnowski, A. J.; Van Heuvelen, K. M.; Münck, E.; Que, L., Jr. Spectroscopic Identification of an Fe^{III} Center, not Fe^{IV} , in the Crystalline Sc–O–Fe Adduct Derived from $[\text{Fe}^{\text{IV}}(\text{O})(\text{TMC})]^{2+}$. *J. Am. Chem. Soc.* **2015**, 137, 3478–3481.

(52) MacMillan, S. N.; Lancaster, K. M. X-ray Spectroscopic Interrogation of Transition-Metal-Mediated Homogeneous Catalysis: Primer and Case Studies. *ACS Catal.* **2017**, 7, 1776–1791.

(53) Pestovsky, O.; Stoian, S.; Bominaar, E. L.; Shan, X. P.; Münck, E.; Que, L., Jr.; Bakac, A. Aqueous $\text{Fe}^{\text{IV}}=\text{O}$: Spectroscopic Identification and Oxo-Group Exchange. *Angew. Chem., Int. Ed.* **2005**, 44, 6871–6874.

(54) Jackson, T. A.; Rohde, J.-U.; Seo, M. S.; Sastri, C. V.; DeHont, R.; Stubna, A.; Ohta, T.; Kitagawa, T.; Münck, E.; Nam, W.; Que, L., Jr. Axial Ligand Effects on the Geometric and Electronic Structures of Nonheme Oxoiron(IV) Complexes. *J. Am. Chem. Soc.* **2008**, 130, 12394–12407.

(55) Scarrow, R. C.; Trimitsis, M. G.; Buck, C. P.; Grove, G. N.; Cowling, R. A.; Nelson, M. J. X-ray Spectroscopy of the Iron Site in Soybean Lipoxygenase-1: Changes in Coordination upon Oxidation or Addition of Methanol. *Biochemistry* **1994**, 33, 15023–15035.

(56) Berry, J. F.; Bill, E.; Garcia-Serres, R.; Neese, F.; Weyhermüller, T.; Wieghardt, K. Effect of N-Methylation of Macrocyclic Amine Ligands on the Spin State of Iron(III): A Tale of Two Fluoro Complexes. *Inorg. Chem.* **2006**, 45, 2027–2037.

(57) Verma, P.; Varga, Z.; Klein, J. E. M. N.; Cramer, C. J.; Que, L.; Truhlar, D. G. Assessment of electronic structure methods for the determination of the ground spin states of Fe(II), Fe(III) and Fe(IV) complexes. *Phys. Chem. Chem. Phys.* **2017**, 19, 13049–13069.

(58) Goldsmith, C. R.; Jonas, R. T.; Stack, T. D. P. C–H Bond Activation by a Ferric Methoxide Complex: Modeling the Rate-Determining Step in the Mechanism of Lipoxygenase. *J. Am. Chem. Soc.* **2002**, 124, 83–96.

(59) Goldsmith, C. R.; Stack, T. D. P. Hydrogen Atom Abstraction by a Mononuclear Ferric Hydroxide Complex: Insights into the Reactivity of Lipoxygenase. *Inorg. Chem.* **2006**, 45, 6048–6055.

(60) Wang, C.-C.; Chang, H.-C.; Lai, Y.-C.; Fang, H.; Li, C.-C.; Hsu, H.-K.; Li, Z.-Y.; Lin, T.-S.; Kuo, T.-S.; Neese, F.; Ye, S.; Chiang, Y.-W.; Tsai, M.-L.; Liaw, W.-F.; Lee, W.-Z. A Structurally Characterized Nonheme Cobalt–Hydroperoxo Complex Derived from Its Superoxo Intermediate via Hydrogen Atom Abstraction. *J. Am. Chem. Soc.* **2016**, 138, 14186–14189.

(61) Wijeratne, G. B.; Corzine, B.; Day, V. W.; Jackson, T. A. Saturation Kinetics in Phenolic O–H Bond Oxidation by a Mononuclear Mn(III)–OH Complex Derived from Dioxygen. *Inorg. Chem.* **2014**, 53, 7622–7634.

(62) Gao, H.; Groves, J. T. Fast Hydrogen Atom Abstraction by a Hydroxo Iron(III) Porphyrin. *J. Am. Chem. Soc.* **2017**, 139, 3938–3941.

(63) Porter, T. R.; Mayer, J. M. Radical reactivity of the Fe(III)/(II) tetramesitylporphyrin couple: hydrogen atom transfer, oxyl radical dissociation, and catalytic disproportionation of a hydroxylamine. *Chem. Sci.* **2014**, 5, 372–380.

(64) Wijeratne, G. B.; Day, V. W.; Jackson, T. A. O–H bond oxidation by a monomeric Mn^{III}–OME complex. *Dalton Trans.* **2015**, 44, 3295–3306.

- (65) Rice, D. B.; Wijeratne, G. B.; Burr, A. D.; Parham, J. D.; Day, V. W.; Jackson, T. A. Steric and Electronic Influence on Proton-Coupled Electron-Transfer Reactivity of a Mononuclear Mn(III)-Hydroxo Complex. *Inorg. Chem.* **2016**, *55*, 8110–8120.
- (66) Coggins, M. K.; Brines, L. M.; Kovacs, J. A. Synthesis and Structural Characterization of a Series of Mn^{III}OR Complexes, Including a Water-Soluble Mn^{III}OH That Promotes Aerobic Hydrogen-Atom Transfer. *Inorg. Chem.* **2013**, *52*, 12383–12393.
- (67) Usharani, D.; Lacy, D. C.; Borovik, A. S.; Shaik, S. Dichotomous Hydrogen Atom Transfer vs Proton-Coupled Electron Transfer During Activation of X–H Bonds (X = C, N, O) by Nonheme Iron–Oxo Complexes of Variable Basicity. *J. Am. Chem. Soc.* **2013**, *135*, 17090–17104.
- (68) Warren, J. J.; Tronic, T. A.; Mayer, J. M. Thermochemistry of Proton-Coupled Electron Transfer Reagents and its Implications. *Chem. Rev.* **2010**, *110*, 6961–7001.
- (69) Weinberg, D. R.; Gagliardi, C. J.; Hull, J. F.; Murphy, C. F.; Kent, C. A.; Westlake, B. C.; Paul, A.; Ess, D. H.; McCafferty, D. G.; Meyer, T. J. Proton-Coupled Electron Transfer. *Chem. Rev.* **2012**, *112*, 4016–4093.
- (70) Hammes-Schiffer, S. Proton-Coupled Electron Transfer: Moving Together and Charging Forward. *J. Am. Chem. Soc.* **2015**, *137*, 8860–8871.
- (71) Cho, K.-B.; Kim, E. J.; Seo, M. S.; Shaik, S.; Nam, W. Correlating DFT-Calculated Energy Barriers to Experiments in Nonheme Octahedral Fe^{IV}O Species. *Chem. - Eur. J.* **2012**, *18*, 10444–10453.
- (72) Fiedler, A. T.; Halfen, H. L.; Halfen, J. A.; Brunold, T. C. Synthesis, Structure Determination, and Spectroscopic/Computational Characterization of a Series of Fe(II)–Thiolate Model Complexes: Implications for Fe–S Bonding in Superoxide Reductases. *J. Am. Chem. Soc.* **2005**, *127*, 1675–1689.
- (73) McDonald, A. R.; Bukowski, M. R.; Farquhar, E. R.; Jackson, T. A.; Koehntop, K. D.; Seo, M. S.; De Hont, R. F.; Stubna, A.; Halfen, J. A.; Münck, E.; Nam, W.; Que, L., Jr. Sulfur versus Iron Oxidation in an Iron-Thiolate Model Complex. *J. Am. Chem. Soc.* **2010**, *132*, 17118–17129.
- (74) Sastri, C. V.; Park, M. J.; Ohta, T.; Jackson, T. A.; Stubna, A.; Seo, M. S.; Lee, J.; Kim, J.; Kitagawa, T.; Münck, E.; Que, L., Jr.; Nam, W. Axial Ligand Substituted Nonheme Fe^{IV}=O Complexes: Observation of Near-UV LMCT Bands and Fe = O Raman Vibrations. *J. Am. Chem. Soc.* **2005**, *127*, 12494–12495.
- (75) Hodges, K. D.; Wollmann, R. G.; Kessel, S. L.; Hendrickson, D. N.; Van Derveer, D. G.; Barefield, E. K. Preparations and Properties of Nitrosyl Complexes of Iron Tetramethylcyclam. X-ray Structures of [Fe(C₁₄H₃₂N₄)NO](BF₄)₂, a *S* = 3/2–1/2 Spin-Equilibrium Complex, and [Fe(C₁₄H₃₂N₄)(NO)(OH)](ClO₄)₂·CH₃CN. *J. Am. Chem. Soc.* **1979**, *101*, 906–917.
- (76) Wilson, S. A.; Chen, J.; Hong, S.; Lee, Y.-M.; Clemancey, M.; Garcia-Serres, R.; Nomura, T.; Ogura, T.; Latour, J.-M.; Hedman, B.; Hodgson, K. O.; Nam, W.; Solomon, E. I. [Fe^{IV}=O(TBC)-(CH₃CN)]²⁺: Comparative Reactivity of Iron(IV)-Oxo Species with Constrained Equatorial Cyclam Ligation. *J. Am. Chem. Soc.* **2012**, *134*, 11791–11806.
- (77) Fang, H.; Ge, H.; Brothers, P. J.; Fu, X.; Ye, S. The Mechanism of E–H (E = N, O) Bond Activation by a Germanium Corrole Complex: A Combined Experimental and Computational Study. *J. Am. Chem. Soc.* **2015**, *137*, 7122–7127.
- (78) Anslyn, E. V.; Dougherty, D. A. *Modern Physical Organic Chemistry*; University Science Books: Sausalito, CA, 2006.
- (79) Watt, C. I. F. Primary kinetic hydrogen isotope effects in deprotonations of carbon acids. *J. Phys. Org. Chem.* **2010**, *23*, 561–571.
- (80) Lehnert, N.; Solomon, E. I. Density-functional investigation on the mechanism of H-atom abstraction by lipoxygenase. *J. Biol. Inorg. Chem.* **2003**, *8*, 294–305.
- (81) Fukuzumi, S. Proton-Coupled Electron Transfer of Unsaturated Fatty Acids and Mechanistic Insight into Lipoxygenase. *Helv. Chim. Acta* **2006**, *89*, 2425–2440.
- (82) Soudackov, A. V.; Hammes-Schiffer, S. Proton-coupled electron transfer reactions: analytical rate constants and case study of kinetic isotope effects in lipoxygenase. *Faraday Discuss.* **2016**, *195*, 171–189.
- (83) Yu, T.; Soudackov, A. V.; Hammes-Schiffer, S. Computational Insights into Five- versus Six-Coordinate Iron Center in Ferrous Soybean Lipoxygenase. *J. Phys. Chem. Lett.* **2016**, *7*, 3429–3433.
- (84) Soudackov, A. V.; Hammes-Schiffer, S. Probing Nonadiabaticity in the Proton-Coupled Electron Transfer Reaction Catalyzed by Soybean Lipoxygenase. *J. Phys. Chem. Lett.* **2014**, *5*, 3274–3278.
- (85) Hatcher, E.; Soudackov, A. V.; Hammes-Schiffer, S. Proton-Coupled Electron Transfer in Soybean Lipoxygenase: Dynamical Behavior and Temperature Dependence of Kinetic Isotope Effects. *J. Am. Chem. Soc.* **2007**, *129*, 187–196.
- (86) Hatcher, E.; Soudackov, A. V.; Hammes-Schiffer, S. Proton-Coupled Electron Transfer in Soybean Lipoxygenase. *J. Am. Chem. Soc.* **2004**, *126*, 5763–5775.
- (87) Offenbacher, A. R.; Hu, S.; Poss, E. M.; Carr, C. A. M.; Scouras, A. D.; Prigozhin, D. M.; Iavarone, A. T.; Palla, A.; Alber, T.; Fraser, J. S.; Klinman, J. P. Hydrogen–Deuterium Exchange of Lipoxygenase Uncovers a Relationship between Distal, Solvent Exposed Protein Motions and the Thermal Activation Barrier for Catalytic Proton-Coupled Electron Tunneling. *ACS Cent. Sci.* **2017**, *3*, 570–579.
- (88) Hu, S.; Soudackov, A. V.; Hammes-Schiffer, S.; Klinman, J. P. Enhanced Rigidification within a Double Mutant of Soybean Lipoxygenase Provides Experimental Support for Vibronically Non-adiabatic Proton-Coupled Electron Transfer Models. *ACS Catal.* **2017**, *7*, 3569–3574.